Numerical Analysis of Heat Transfer in Annulus of Composite Material at Different Operation Conditions.

Amina Hmoud Alikhan[1]*, Hadi Obaid Mery[1], Osamah Malik Mohammed[1]

Abstract

The current study aims to numerically examine the impact of the radius ratio of a three-dimensional annulus,, and the direction of support fiber array arrangement on heat transfer employing two distinct methods to optimize effective thermal conductivity: minimizing and maximizing. The annulus was manufactured from graphite/epoxy laminated composite material. Constant walls temperature boundary condition and steady-state conditions were applied to the system with 0.2, 0.3, 0.4, and 0.5 different radius ratios, inclination angles (0° and 90°), and modified Rayleigh number "Ra*" ranged from 10 to 500. The results found that the Nusselt number decreased for all parameters as the radius ratio Rr decreased, indicating a wider cold outer cylinder gap. For large values of the modified Rayleigh number, the average Nu number "Nu_{avg}." decreases with an increase in "δ", and increases with a rise in the modified Rayleigh number; for low values of "Ra*", δ has no effect. For horizontal, and vertical states $\delta=0^o$, and $\delta=90^o$ respectively, at higher and lower thermal conductivity, the divergence of the average Nusselt is 5.1% and 10%, respectively. In a horizontal cylinder adding fins on the inner cylinder is more substantial due to its impeding effect, and Nu_L increases with the cylinder length.

الخلاصة:

هدف الدراسة الحالية إلى فحص تأثير نسبة نصف قطر الحلقة ثلاثية الأبعاد واتجاه ترتيب مجموعة الألياف الداعمة على انتقال الحرارة رقميًا باستخدام طريقتين متميزتين لتحسين التوصيل الحراري الفعال: التقليل والتعظيم. تم تصنيع الحلقة من مادة مركبة مغلفة بالجرافيت / الإيبوكسي. تم تطبيق حالة حدود درجة حرارة الجدران الثابتة وظروف الحالة المستقرة على النظام بنسب نصف قطر مختلفة 0.2 و 0.3 و 0.4 و 0.5 وزوايا ميل (0° و 90°) ورقم رايلي المعدل " Ra* " يتراوح من 10 إلى 500 وجدت النتائج أن رقم نوسلت انخفض لجميع المعلمات مع انخفاض نسبة نصف القطر Rr، مما يشير إلى فجوة أسطوانية خارجية باردة أوسع. بالنسبة للقيم الكبيرة لرقم رايلي المعدل، ينخفض متوسط "Nu_{avg}" مع زيادة δ، ويزداد مع ارتفاع رقم رايلي المعدل؛ بالنسبة للقيم المنخفضة لـ " Ra* " لا يوجد تأثير لـ δ. بالنسبة للحالات الأفقية والرأسية $\delta=0^o$ و 90° على التوالي وعند الموصلية الحرارية الأعلى والأدنى يكون تباعد متوسط نوسلت 5.1٪ و 10٪ على التوالي. في الأسطوانة الأفقية، يكون إضافة الزعانف على الأسطوانة الداخلية أكثر أهمية بسبب تأثيرها المعيق للجريان، ويزداد Nu المحلي مع طول الأسطوانة.

1. INTRODUCTION

Fiber-reinforced multilayer composite materials are highly desirable in modern engineering applications due to their numerous advantages over most other materials, including their high strength-to-density ratio, stiffness-to-density ratio, high corrosion resistance, and plasticity. The majority of these special benefits stem from two characteristics of these materials: integrating diverse physical, mechanical, and thermal capabilities of different materials and having the capacity to alter the orientations of the fibers in every layer to meet the requirements of the layout. In many designs, composite materials are employed to lighten and enhance the characteristics of different

constructions. Many industrial uses, such as electronic cooling, satellites, pipes, and aerospace components, have led to the development of composite materials. Among their numerous advantageous qualities are high ratios of strength to weight and robust corrosion resistance. The characteristics of these materials for use in the construction of structural parts have been examined by many engineers and researchers [1].

Numerous scientists and engineers investigated the characteristics of different materials as well as the challenges associated with creating structural components made of them [2–4]. Any characteristic of a composite consisting of more than one material is valuable. However, a composite's geometrical structure also plays a role in determining the final value of the quality of the composite as a whole. These end attributes are frequently referred to as a composite's effective properties. Composites are relatively affected by temperature and not be sensitive to thermal conductivity, leading to good heat insulation, which are the characteristics of modern composites for engineering applications [5–9].

 For the first time, Norouzi et al. [10] provided an exact mathematical solution for constant conductive heat transport in multilayer spherical fiber-reinforced composite laminates. The orthotropic temperature distribution of the laminate was determined under general linear boundary conditions, which are appropriate for various scenarios including combinations of conduction, convection, and radiation both inside and outside of the sphere. Between the laminas, the temperature and heat flux continuity were applied. The separation of variables approach was used to get an exact answer, and the recursive Thomas algorithm was utilized to solve the set of equations about the coefficient of the Fourier-Legendre series of temperature distribution. Sandwich construction was designed as a thermal management technique with greater thermal conductivity and structural stability by Sangwook et al. [11] Improving the interface between the stages and the heat conductivity of each sandwich-building phase was prioritized. Mechanical and thermal characteristics of an available carbon foam commercially were assessed Anisotropy and property change were noted in carbon foam with graphitic properties. It was shown that the best construction among those evaluated could be achieved by reducing the adhesive layer's thickness between the face sheets.

Kang et al. [12] Used filler has a tube shape to create an analytical model to explain the transport in as a composite membrane, taking into account the several operational and structural features of the composite membrane. A two-dimensional analytical solution of transient composite heat conduction was obtained by Wang et al. [13], the transient temperature fields were developed using the separation of variables method where the analytical solution included the Bessel series and the trigonometric series in polar coordinates, the trigonometric series consisted of both the sine and cosine series and the initial parameter approach was applied to deal with the continuity conditions at the interfaces. The solution can be obtained simply by operating two matrices, Laplace transform was omitted, the solution process was carried out directly in the time domain, and the effect of the fiber angle on the transient thermal conductivity properties was also considered. Gaosheng et al. [14] Used different wavelengths of Fourier transform infrared spectrometer (FTIR) in the presence of a xonotlite– silica aerogel composite materials to study their effect on heat transfer; the findings demonstrate that the samples' spectrum extinction coefficients are very wavelength dependent, with rising temperatures, all of the samples' total Rosseland mean extinction coefficients fall. As sample densities rise, the radiative conductivities decrease approximately proportionally to the temperature cube.

In this study, a concentric annulus at a different position filled with fiber arranged at different directions, which serves as a heat exchanger is employed to examine natural convection heat transfer. It was looked into how the radius ratio affected things. As a function of effective thermal conductivity, two forms of optimization will be carried out: thermal conductivity maximization and minimization. Modified Rayleigh numbers ranging from 10 to 500 and different radius ratios ranging from 0.2 to 0.5 at horizontal and vertical states have been impacted by the study.

2. Mathematical Model

The mathematical model represents the use of Boussinesq's approximation, and Darcy flow model steady-state equations of the mass, momentum, and energy conservation rules to simulate the incompressible porous media flow. [15] Provides these equations in vectorial notation.

Fig. 1 depicts the schematic drawing of the geometry and Cartesian coordinate system used to solve the problem.
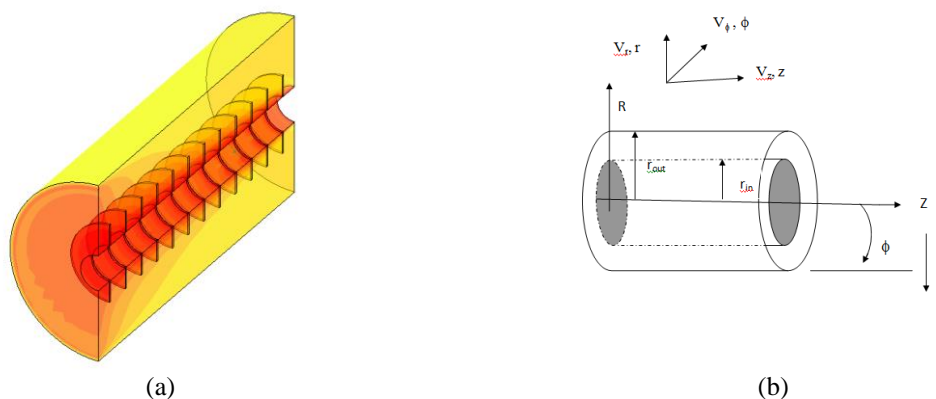
(a)   (b)

Fig. 1 Geometry and coordinates system

3. Governing Equations

Steady state conservation equations for mass, momentum, and energy are as follows:

$$\rho = \rho_2\{1 - \beta(T - T_2)\} \tag{1}$$

$$\beta = \frac{1}{\rho}\frac{\partial \rho}{\partial T} \tag{2}$$

β : Which the thermal factor of volume expansion, measured at T_2, the temperature at which the outer cylinder's inner surface is at. The density at T_2 is represented by ρ_2, while the density at T is by ρ [16].

3.1 Mass Conservation

$$\frac{\partial u_r}{\partial r} + \frac{u_r}{r} + \frac{1}{r}\frac{\partial u_\emptyset}{\partial \emptyset} + \frac{\partial u_z}{\partial z} \tag{3}$$

3.2 Momentum Equations

The Darcy flow model is the most often utilized model for flow in porous media. According to Darcy's law, the pressure gradient and the volume average velocity through a porous medium are proportional. The Darcy's model [17] for three-dimensional flows is:

1. Radial Momentum Equation

$$u_r = \frac{K}{\mu_f}\left[-\frac{\partial p}{\partial r} - \rho \, g \, cos\emptyset \, cos\delta\right] \tag{4}$$

2. Angular Momentum Equation

$$u_\emptyset = \frac{K}{\mu_f}\left[-\frac{\partial p}{\partial \emptyset} + \rho \, g \, sin\emptyset \, cos\delta\right] \tag{5}$$

3. Momentum Equation in Axial Direction

$$u_z = \frac{K}{\mu_f}\left[-\frac{\partial p}{\partial z} - \rho \, g \, sin\delta\right] \tag{6}$$

3.3 Energy Equation

$$\frac{\partial(\rho \, c_p \, T)}{\partial t} + u_r\frac{\partial(\rho \, c_p \, T)}{\partial r} + \frac{u_\emptyset}{r}\frac{\partial(\rho \, c_p \, T)}{\partial \emptyset} + u_z\frac{\partial(\rho \, c_p \, T)}{\partial z} = \frac{1}{r}\frac{\partial}{\partial r}\left\{r\frac{\partial(k \, T)}{\partial r}\right\} + \frac{1}{r^2}\frac{\partial^2(k \, T)}{\partial \emptyset^2} + \frac{\partial^2(k \, T)}{\partial z^2} + \mu \, \Phi \tag{7}$$

Where Φ : is viscous dissipation function [18].

3.4 Fin Equation

The energy equation for the fin itself is:

$$\frac{\partial T}{\partial r} + \frac{T}{r} + \frac{1}{r}\frac{\partial T}{\partial \theta} + \frac{\partial T}{\partial z} = 0 \tag{8}$$

As in [19] Ω and, Ψ represent the vortex and potential vectors with their components respectively:
Ψ $as\ a\ fuction\ of\ r, \emptyset, and\ z$ Defined by:

$$U = \alpha_{eff.}\ \nabla\ X\ \Psi \tag{9}$$

$$\nabla^2 \psi_r = \frac{1}{R}\frac{\partial U_z}{\partial \emptyset} - \frac{\partial U_\emptyset}{\partial Z} \tag{10}$$

$$\nabla^2 \psi_\emptyset = \frac{\partial U_r}{\partial Z} - \frac{\partial U_z}{\partial R} \tag{11}$$

$$\nabla^2 \psi_z = \frac{1}{R}\frac{\partial(RU_\emptyset)}{\partial R} - \frac{1}{R}\frac{\partial U_r}{\partial \emptyset} \tag{12}$$

4. Non Dimensional Variables

In order to use dimensionless form instead of the governing equations, the dimensionless magnitudes need to be specified as follows: r_2 is the specific length [16].

$$R = \frac{r}{r_2}, \qquad Z = \frac{z}{r_2}, \qquad U_r = \frac{u_r\ l}{\alpha_{eff.}}, \qquad U_\emptyset = \frac{u_\emptyset\ l}{\alpha_{eff.}}, U_z = \frac{u_z\ l}{\alpha_{eff.}}$$

$$\theta = \frac{(T - T_2)}{(T_1 - T_2)}, \qquad P = \frac{p\ K\ l}{\alpha_{eff.}\ \mu_f\ r_2}, \qquad R_a^* = \frac{g\ \beta\ K(T_1 - T_2)(r_2 - r_1)}{\alpha_{eff.}\ \vartheta}$$

$$S_1 = \frac{s}{2r_2}, \qquad S_2 = \frac{\frac{s}{2} + t}{r_2}, H_1 = \frac{H_f}{r_2}$$

Replace these dimensionless magnitudes in the governing equations. There are other ways to express equation (3) in terms of ψ_r, ψ_ϕ and ψ_z as :

$$U_r = \left(\frac{1}{R}\frac{\partial \psi_z}{\partial \emptyset} - \frac{\partial \psi_\emptyset}{\partial Z}\right) \tag{13}$$

$$U_\emptyset = \left(\frac{\partial \psi_r}{\partial Z} - \frac{\partial \psi_z}{\partial R}\right) \tag{14}$$

$$U_z = \frac{1}{R}\left(\frac{\partial(R\psi_\emptyset)}{\partial R} - \frac{\partial \psi_r}{\partial \emptyset}\right) \tag{15}$$

The momentum equations will be as follows after taking the curl of momentum equations to remove pressure terms:

$$R_a^* \frac{l}{(r_2 - r_1)}\left(\frac{1}{R}\sin\delta\ \frac{\partial\theta}{\partial\emptyset} + \sin\emptyset\ \emptyset\ cos\delta\ \frac{\partial\theta}{\partial Z}\right) = -\frac{\partial^2\psi_r}{\partial R^2} - \frac{1}{R^2}\frac{\partial(R\psi_r)}{\partial R} - \frac{2}{R}\frac{\partial\psi_r}{\partial R} - \frac{1}{R^2}\frac{\partial^2\psi_r}{\partial\emptyset^2} - \frac{\partial^2\psi_r}{\partial Z^2} - \frac{2}{R}\frac{\partial\psi_z}{\partial Z} \tag{16}$$

$$R_a^* \frac{l}{(r_2 - r_1)}\left(\cos\emptyset\ \cos\delta\ \frac{\partial\theta}{\partial Z} - sin\delta\ \frac{\partial\theta}{\partial R}\right) = -\frac{\partial^2\psi_\emptyset}{\partial Z^2} - \frac{\partial^2\psi_\emptyset}{\partial R^2} - \frac{1}{R^2}\frac{\partial^2\psi_\emptyset}{\partial\emptyset^2} - \frac{2}{R^2}\frac{\partial\psi_r}{\partial\emptyset} + \frac{\psi_\emptyset}{R^2} - \frac{1}{R}\frac{\partial\psi_\emptyset}{\partial R} \tag{17}$$

$$R_a^* \frac{l}{(r_2 - r_1)}cos\delta\left(\frac{1}{R}\cos\emptyset\ \frac{\partial\theta}{\partial\emptyset} + \sin\emptyset\ \frac{\partial\theta}{\partial R}\right) = -\frac{\partial^2\psi_z}{\partial R^2} - \frac{1}{R}\frac{\partial\psi_z}{\partial R} - \frac{1}{R^2}\frac{\partial^2\psi_z}{\partial\emptyset^2} - \frac{\partial^2\psi_z}{\partial Z^2} \tag{18}$$

The energy equation is going to be:

$$\left(\frac{1}{R}\frac{\partial\psi_z}{\partial\emptyset} - \frac{\partial\psi_\emptyset}{\partial Z}\right)\frac{\partial\theta}{\partial R} + \frac{1}{R}\left(\frac{\partial\psi_r}{\partial Z} - \frac{\partial\psi_z}{\partial R}\right)\frac{\partial\theta}{\partial\emptyset} + \left(\frac{\psi_\emptyset}{R} + \frac{\partial\psi_\emptyset}{\partial R} - \frac{1}{R}\frac{\partial\psi_r}{\partial\emptyset}\right)\frac{\partial\theta}{\partial Z} = \frac{l}{r_1}\left(\frac{\partial^2\theta}{\partial R^2} + \frac{1}{R}\frac{\partial\theta}{\partial R} + \frac{1}{R^2}\frac{\partial^2\theta}{\partial\emptyset^2} + \frac{\partial^2\theta}{\partial Z^2}\right) \tag{19}$$

The fin equation is as follow:

$$\frac{\partial\theta}{\partial R} + \frac{\theta}{R} + \frac{1}{R}\frac{\partial\theta}{\partial\emptyset} + \frac{\partial\theta}{\partial Z} = 0 \tag{20}$$

4.1 Hydraulic Boundary Conditions with Dimensionless form

The boundary conditions with Hydraulic Dimensionless form are:

$$at\ R = R_1, 1 \xrightarrow{yields} \frac{1}{R}\frac{\partial(R\psi_r)}{\partial R} = \psi_\emptyset = \psi_z = 0$$

$$at\ \emptyset = 0, \pi \xrightarrow{yields} \psi_r = \frac{\partial \psi_\emptyset}{\partial \emptyset} = \psi_z = 0$$

$$at\ Z = 0, L \xrightarrow{yields} \psi_r = \psi_\emptyset = \frac{\partial \psi_z}{\partial Z} = 0$$

The fin boundary condition is:

$$\frac{1}{R}\frac{\partial(R\psi_r)}{\partial R} = \frac{\partial \psi_\emptyset}{\partial \emptyset} = \frac{\partial \psi_z}{\partial Z} = 0$$

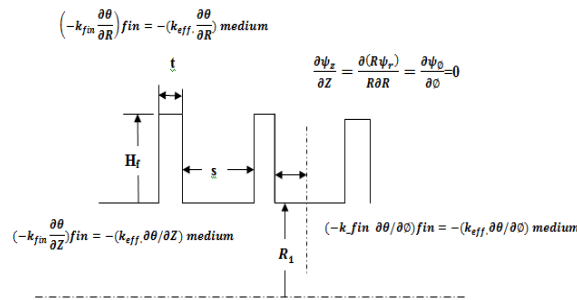For fin base: at $R = R_1$ *for* $\phi = 0, \pi$ as in Fig.

For fin tip: at $r = r_1 + H_f$ *for* $\phi = 0, \pi$

Fig. 2: boundary conditions of fins**.**

4.2 Thermal Boundary Conditions with Dimensionless form

Dimensionless form of the boundary conditions for the temperature field are:

$$at\ R = R_1 = \frac{r_1}{r_2} \xrightarrow{yields} \theta = 1$$

$$at\ R = R_2 = 1 \xrightarrow{yields} \theta = 0$$

$$at\ \emptyset = 0, \pi \xrightarrow{yields} \frac{\partial \theta}{\partial \emptyset} = 0$$

$$at\ Z = 0, L \xrightarrow{yields} \frac{\partial \theta}{\partial Z} = 0$$

$$at\ R = H_1 \xrightarrow{yields} -k_{fin}\frac{\partial \theta}{\partial R}\Big|_{fin} = -k_{eff}\frac{\partial \theta}{\partial R}\Big|_{medium}$$

at S_1 *for any R and* $\emptyset$ *and*

at S_2 *for any R and* $\emptyset$

$$-k_{fin}\frac{\partial \theta}{\partial Z}\Big|_{fin} = -k_{eff}\frac{\partial \theta}{\partial Z}\Big|_{medium}$$

at $\emptyset = 0, \pi$ *and any R*

$$-k_{fin}\frac{\partial \theta}{\partial \emptyset}\Big|_{fin} = -k_{eff}\frac{\partial \theta}{\partial \emptyset}\Big|_{medium}$$

$$k_{eff} = (1 - \varepsilon)\,k_s + \varepsilon\,k_f \tag{21}$$

The direction of the fiber can also affect heat conduction. Heat conduction would be at its lowest when the fiber axis is perpendicular to the heat flux. The maximum conductivity occurs when the fiber and the heat stream are parallel. The conductive heat transfer coefficients of epoxy and graphite fibers are 0.19 W/m K and 14.74 W/m K,

respectively. The graphite fibers' and the epoxy matrix's conductivity coefficients are very different from one another. As a result, this composite laminate's heat conductivity is significantly higher when it runs parallel to the fibers than when it runs perpendicular to them. The thermal conductivity of "graphite/epoxy composite" is (11.1, and 0.87) W/m K in the parallel, and perpendicular fibers, with a volumetric percentage of 75 percent [20].

Grid point numbers 21, 31, and 301 utilized in the R, Ø, and Z-directions respectively, will be applied in the current investigation. Equation of convergence provided by inequality:

$$Max \left| \frac{\theta^{n+1} - \theta^n}{\theta^n} \right| \leq 10^{-8}$$

4.3 Calculation of Nu_L, and Nu_{avg}.

From [16] local Nusselt number can be derived which indicates the of surface energy convection rate.

$$Nu = \frac{q(r_2 - r_1)}{k(T_1 - T_2)} \tag{22}$$

The local Nusselt numbers Nu_1 and Nu_2 of outer and inner cylinders are inscribed in the following format [16]:

$$Nu_{Local\ 1} = -(1 - R_1) \left(\frac{\partial \theta}{\partial R} \right)_{R=R_1} \tag{23}$$

$$Nu_{Local\ 2} = -(1 - R_1) \left(\frac{\partial \theta}{\partial R} \right)_{R=R_1} \tag{24}$$

The following is the definition of the average Nusselt numbers Nu_1, and Nu_2, respectively, on the inner and outer cylinders:

$$Nu_1 = -(1 - R_1) \frac{1}{\pi L} \int_0^\pi \int_0^L \left(\frac{\partial \theta}{\partial R} \right)_{R=R_1} dZ\ d\emptyset \tag{25}$$

$$Nu_2 = -(1 - R_1) \frac{1}{\pi L} \int_0^\pi \int_0^L \left(\frac{\partial \theta}{\partial R} \right)_{R=1} dZ\ d\emptyset \tag{26}$$

5. Result and Discussion

The isotherms and streamlines for the two scenarios of the graphite fibers/epoxy's maximum and minimum thermal conductivity, as well as for various conditions are displayed in Fig 3 to Fig 12. For the horizontal annulus, the homogeneity of isothermal lines is evident in Fig 3 and Fig 4. It was also noted that, in Fig 4, the cold zone for Rr = 0.2 is greater due to the wider gap, and the streamline intensity is lower for Rr = 0.5 than for Rr = 0.2. As shown in Fig 5 and Fig 6, greater streamlines occur at the boundaries, and lower values far away from the boundary, which expands and performs bean shape in vertical annulus (δ=90°). In the horizontal position, increasing the Ra* results in a thicker cold layer at the bottom of the wall and an increase in the temperature field at the top of the wall. Fig. 7 and Fig. 8 illustrate how more heat is carried upward and how there is a noticeable temperature differential between the top and bottom portions of the annulus. High-intensity streamlines are found at the bottom and edges, and when δ increases to 90 degrees, the streamlines center with negative-value expands and disappears into the upper region. These Fig.s make it very evident that, for δ=0°, at the cold and hot cylinders, the isothermal lines are almost parallel, suggesting that, at low values of Ra*, heat is transmitted by conduction. The isothermal lines exhibit a distorted conductive pattern and curvilinear shape when they are far from the inner cylinder, suggesting the presence of up-and-down convective flows. These graphs can also demonstrate how the enclosure's inclination angles affect convective heat transfer. As increases of the inclination angle, the enclosure's temperature rises and the convective flow gets more intense, making the constant temperature lines appear more curved. Darcy's law, which demonstrates how the driving force is produced in the enclosure by the gravity acceleration component vector which was in the same flow direction related to both mass density and temperature gradient, is what led to the appearance of this situation. The fluid at a cold surface becomes denser and reflects heat, while the fluid at a hot surface becomes less dense, and absorbs heat. As seen in Fig. 9 and Fig. 10, the isothermal lines for vertical annulus imply high temperature and hence less heat transfers than that for horizontal state. The isotherms and streamlines in Fig. 11 and Fig. 12 at lower studied thermal conductivity "k=0.87 W/m K" (vertical fibers direction) behave similarly to those in earlier Fig.s, albeit with naturally reduced heat transfer. As a result, for k=0.87 W/m K, at the same conditions of modified Rayleigh number, radius ratio, and angle, the bottom region is colder than that in the case of k=11.1 W/m K (parallel fibers direction). At two different values of thermal conductivity 0.87 and 11.1 (W/m K), the average Nusselt number changes with the modified Rayleigh number on the outer and inner cylinders. Horizontal state and various values of radius ratio are depicted in Fig. 13 to Fig. 16. It is evident that Nu increases with an increase in the modified Rayleigh number and decreases with a drop in Rr (bigger gap) for the outer cold cylinder. Fig. 17 and Fig. 18 clearly show the difference between the average Nu in the two scenarios, equivalent to 5.1% for δ=0° and 10% for δ=90°. The average Nusselt number change with modified Rayleigh number on the outer and inner

cylinders, for k=0.87 W/m K and k=11.1 W/m K, respectively, for δ=90º and various Rr values, is depicted in Fig. 19 to Fig. 22. According to these Fig.s, there is less heat transmission than when δ=0º. Fig. 23 to Fig. 30 show the distribution of the local Nusselt number for δ = 0º and δ = 90º, respectively, over the dimensionless cylinder length. The influence of adding fins to the inner cylinder is particularly substantial for δ=0º, as Fig. 23 and Fig. 24 demonstrate. The wavy curve will increase with the increase of the modified Rayleigh number, as Fig. 25 and Fig. 26 demonstrate. The local Nusselt number was lower for k=0.87 W/m K in Fig. 27 to Fig. 38, but it behaved similarly to the earlier findings for k=11.1 W/m. K.

From the numerical data, correlations were inferred, and they are provided as follows:

At thermal conductivity of 11.1W/m K:

$$Nu_{out} = \frac{1.923 \, Ra^{0.176} \, Rr^{0.5667}}{\delta^{0.011}}$$

(27)

At thermal conductivity of 0.87 W/m K:

$$Nu_{out} = \frac{1.67 \, Ra^{0.185} \, Rr^{0.59}}{\delta^{0.013}}$$

(28)
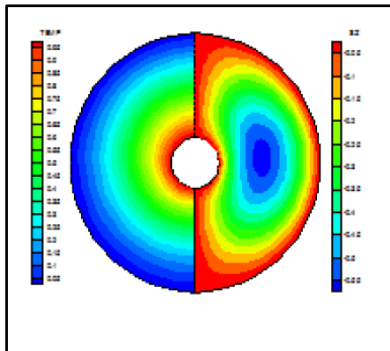
Fig. 3 Temperature and Streamline Visualization for "Rr=0.2 ,Ra*=10, δ=0,k=11.1"
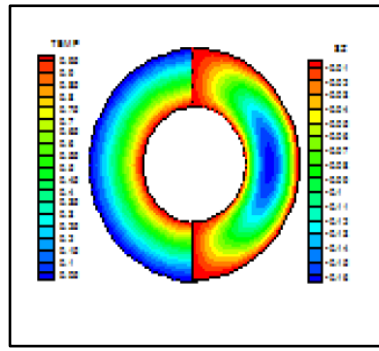
Fig. 4 Temperature and Streamline Visualization for "Rr=0.5 ,Ra*=10, δ=0,k=11.1"
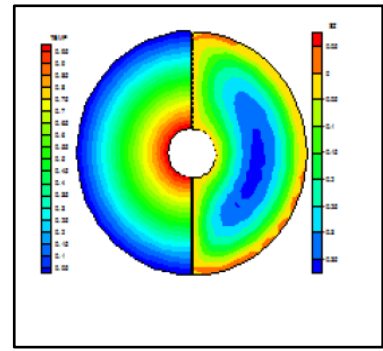
Fig. 5 Temperature and Streamline Visualization for "Rr=0.2 ,Ra*=10, δ=90,k=11.1"
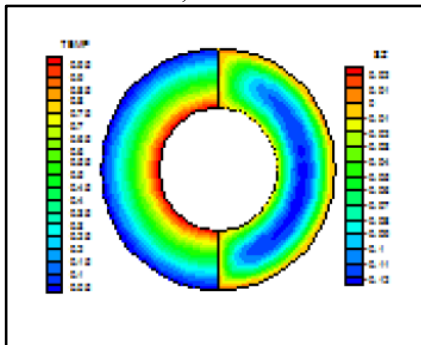
Fig. 6 Temperature and Streamline Visualization for "Rr=0.5 ,Ra*=10, δ=90,k=11.1"
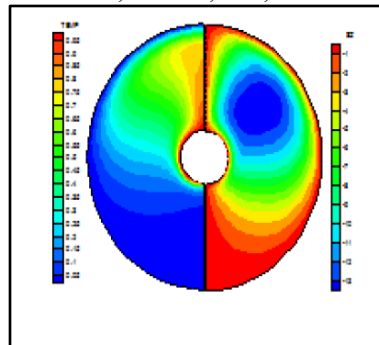
Fig. 7 Temperature and Streamline Visualization for "Rr=0.2 ,Ra*=500, δ=0,k=11.1"
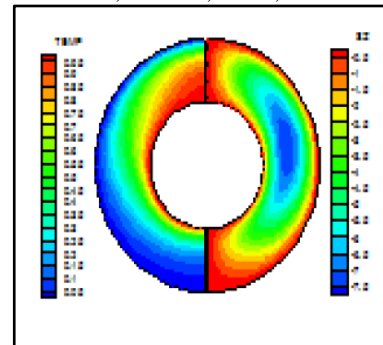
Fig. 8 Temperature and streamline Visualization for "Rr=0.5 ,Ra*=500, δ=0,k=11.1"
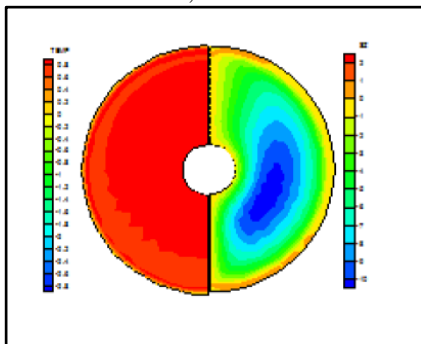
Fig. 9 Temperature and Streamline Visualization for "Rr=0.2 ,Ra*=500, δ=90,k=11.1"
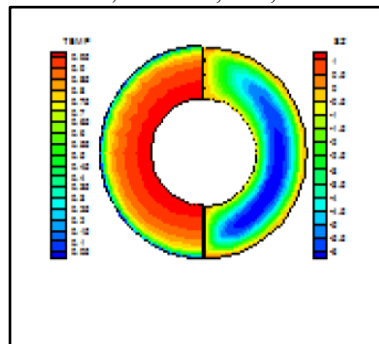
Fig. 10 Temperature and Streamline Visualization for "Rr=0.5 ,Ra*=500, δ=90,k=11.1"
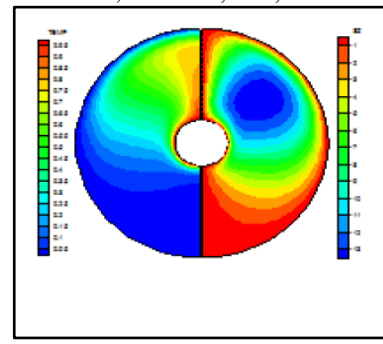
Fig. 11 Temperature and Streamline Visualization for "Rr=0.2 ,Ra*=10, δ=0,k=0.87"
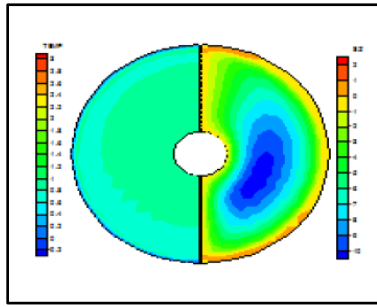
Fig. 1 Temperature and Streamline Visualization for "Rr=0.2 ,Ra*=500, δ=90,k=0.87"
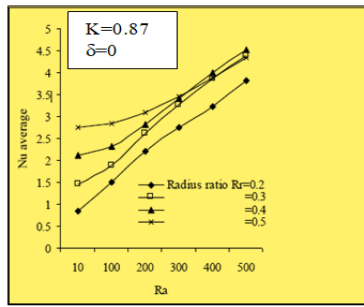
Fig. 2 Average Nusselt number Variation with Rayleigh number of different outer cylinder radius ratio
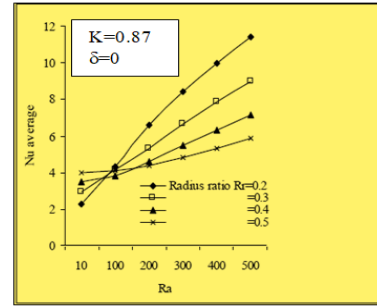
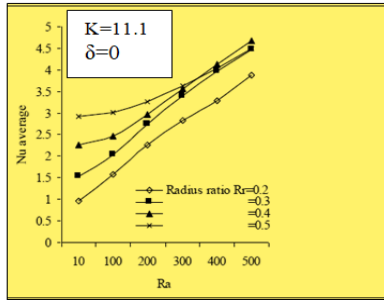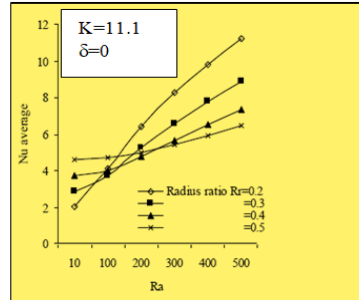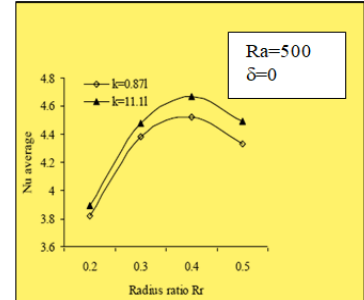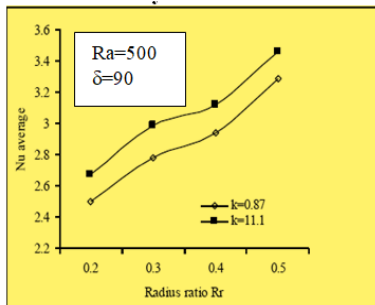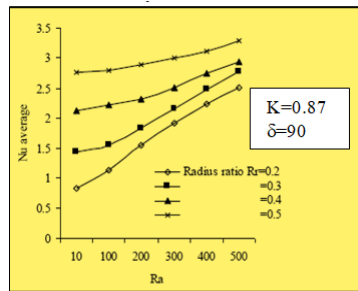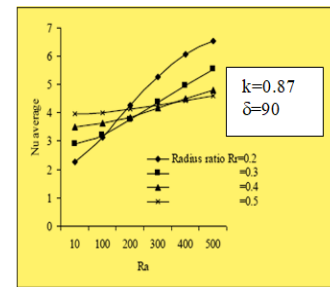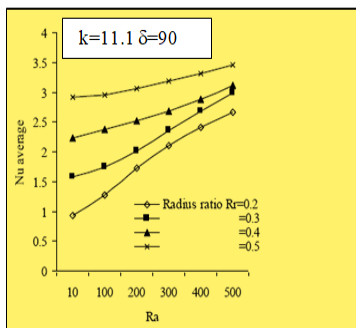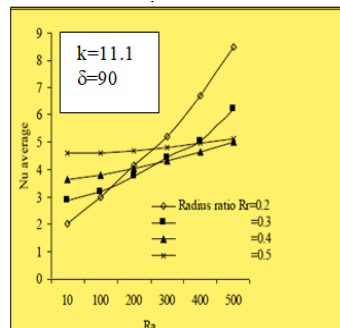Fig. 3 Average Nusselt number Variation with Rayleigh number of different outer cylinder radius ratio

Fig 4 Average Nusselt number Variation with Rayleigh number of different outer cylinder radius ratio

Fig. 5 Average Nusselt number Variation with Rayleigh number of different inner cylinder radius ratio

Fig. 6 Average Nusselt number Variation with different outer cylinder radius ratio

Fig. 7 Average Nusselt number Variation with different outer cylinder radius ratio

Fig. 8 Average Nusselt number Variation with Rayleigh number of different outer cylinder radius ratio

Fig. 20 Average Nusselt number Variation with Rayleigh number of different innee cylinder radius ratio

Fig. 29 Average Nusselt number Variation with Rayleigh number of different outer cylinder radius ratio

Fig. 10 Average Nusselt number Variation with Rayleigh number of different inner cylinder radius ratio
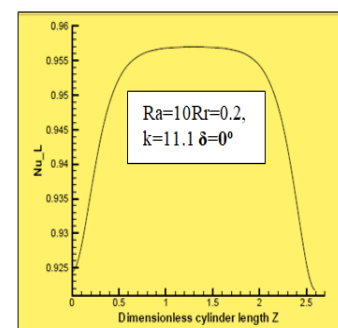

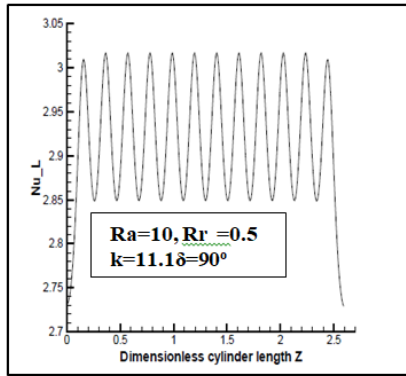Fig. 11 Local Nusselt number Variation with length of cylinder

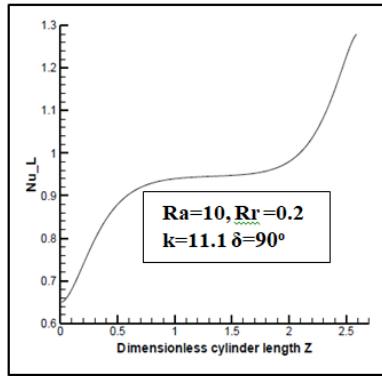Fig. 12 Local Nusselt number Variation with length of cylinder

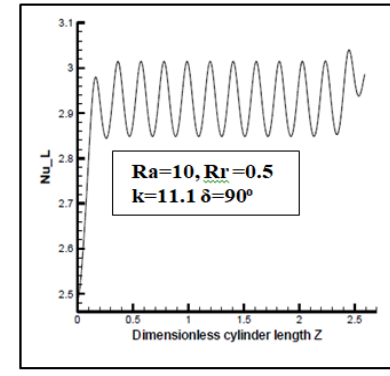Fig. 13 Local Nusselt number Variation with length of cylinder

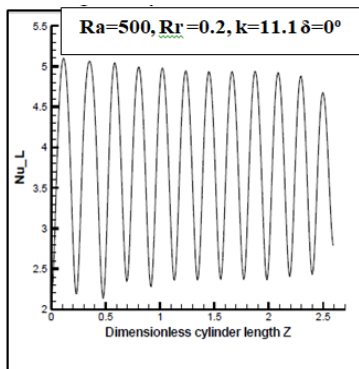Fig. 14 Local Nusselt number Variation with length of cylinder

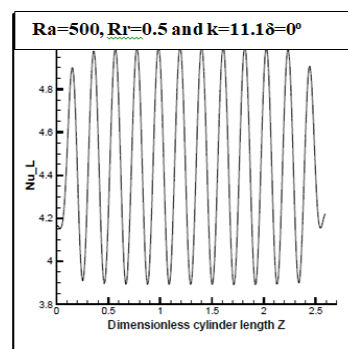Fig. 15 Local Nusselt number Variation with length of cylinder

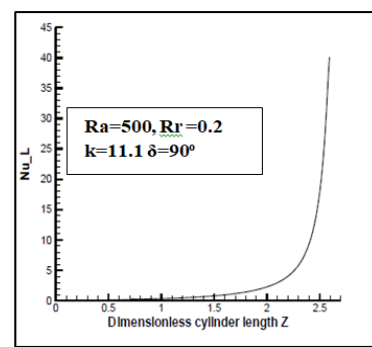Fig. 16 Local Nusselt number Variation with length of cylinder

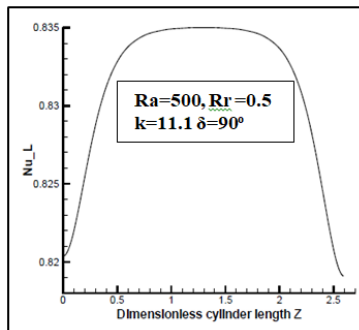Fig. 17 Local Nusselt number Variation with length of cylinder

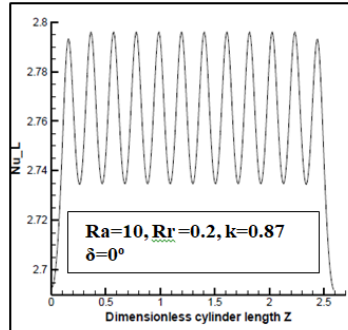Fig. 30 Local Nusselt number Variation with length of cylinder

Fig. 31 Local Nusselt number Variation with length of cylinder
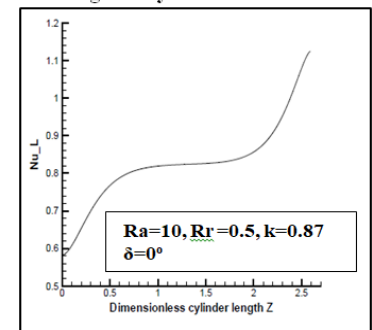

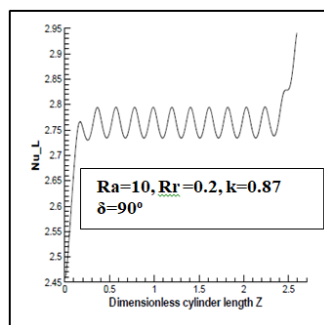Fig. 18 Local Nusselt number Variation with length of cylinder

Fig. 19 Local Nusselt number Variation with length of cylinder
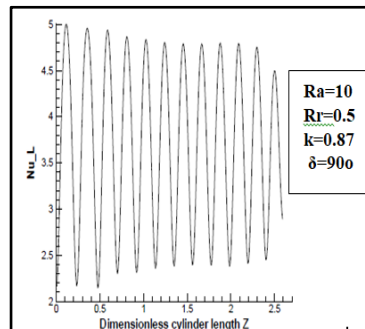

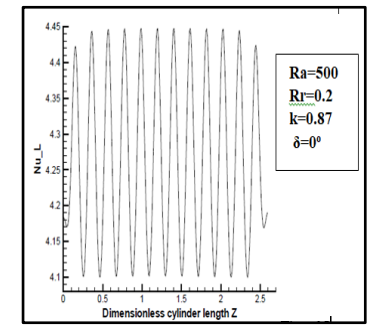Fig. 20 Local Nusselt number Variation with length of cylinder

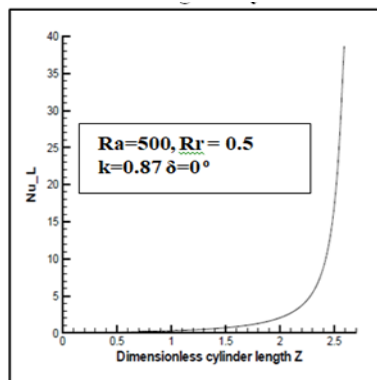Fig. 21 Local Nusselt number Variation with length of cylinder

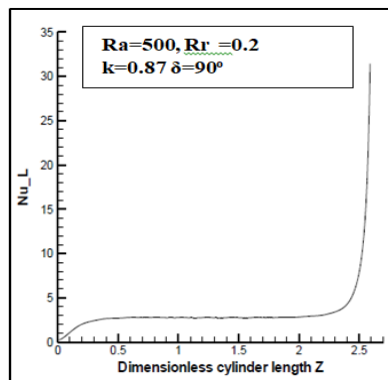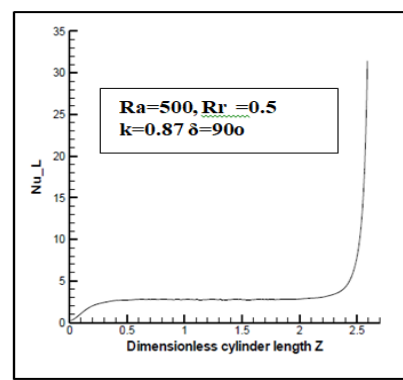| Fig. 22 Local Nusselt number Variation with length of cylinder | Fig. 23 Local Nusselt number Variation with length of cylinder | Fig. 24 Local Nusselt number Variation with length of cylinder |

6. CONCLUSIONS

1. For the outer cold cylinder, the Nusselt number decreased as the radius ratio Rr decreased, indicating a wider gap.
2. For horizontal, and vertical states "δ=0°", and "90°" respectively, the divergence of the average Nusselt is 5.1% and 10%, respectively at higher and lower thermal conductivity.
3. For all studied parameters average Nusselt number declined for high values of the modified Rayleigh number and an increase in angle inclinations; for low values the average Nusselt number increases with an increase in the modified Rayleigh number.
4. The presence of fins on the surface of the inner cylinder has an effect that appears essentially in the horizontal case due to its hindering effect, which leads to an increase in the local Nusselt number, and Nu_L also increases with the increase in the length of the cylinder.

7. Nomenclature

Symbol	Description	Unit	Symbol	Description	Unit
C_p	Specific heat at constant pressure	kJ/kg°C	Nu_{in}	Average Nusselt number on the inner cylinder	-
g	Acceleration due to gravity	m/s^2	Nu_{out}	Average Nusselt number on the outer cylinder	-
H_f	Fin length	m	p	Pressure	N/m^2
k_f	Thermal conductivity of the fluid	W/m K	q	Local heat flux	W
k_s	Thermal conductivity of the solid	W/m K	r	Radial coordinate	m
$K_{eff.}$	Effective thermal conductivity of the porous media	W/m K	R	Dimensionless radial coordinate	m
K	Permeability	m^2	Ra^*	Modified Rayleigh number	-
l	Cylinder length	m	Rr	Radius ratio	-
L	Dimensionless cylinder length	-	S	Fin pitch	m
Nu_1	Local Nusselt number on the inner cylinder	-	T	Temperature	K
Nu_2	Local Nusselt number on the outer cylinder	-	u_r, u_ϕ, u_z	velocity component in r,φ and z - direction	m/s

REFERENCES

1. Yuan B. et al. Heat insulation properties of silica aerogel/glass fiber composites fabricated by press forming // Mater. Lett. 2012. Vol. 75. P. 204–206.
2. Alikhan A.H., Maghrebi M.J. Experimental investigation on frequency pulsation effects on a single pass plate heat exchanger performance // Heat Transf. 2022. Vol. 51, № 3. P. 2688–2701.
3. Alikhan A.H., Kazemi M., Soroush H. Enhanced performance of photovoltaic thermal module and solar thermal flat plate collector connected in series through integration with phase change materials: A comparative study // Therm. Sci. Eng. Prog. Elsevier, 2024. Vol. 47. P. 102305.
4. Alasady A.H., Maghrebi M.J. Characterisation of a plate heat exchanger chevron type with carbon-based nanofluids under pulsed condition // Proc. Inst. Mech. Eng. Part C J. Mech. Eng. Sci. 2022. Vol. 236, № 7. P. 3831–3846.

5. H.Saleh M., H. Dhaef A. Heat Transfer in Inclined Enclosure of Silica Aerogel/Glass Fiber Composite Material // Int. J. Comput. Appl. 2015. Vol. 117, № 8. P. 5–12.

6. Dhaef M.H.S.A.H. Heat Transfer in Horizontal Annulus Saturated with Copper Nanofluid under Various Boundary Conditions // Int. J. Sci. Res. 2015. Vol. 4, № 4. P. 2141–2147.

7. Saleh M.H., Katea A.M. Laminar Free Convection In Horizontal Annulus Filled With Glass Beads And With Annular Fins On The Inner Cylinder // J. Eng. 2023. Vol. 19, № 08. P. 999–1018.

8. Alikhan A.H. et al. Optimal Design Of The Concentric Annulus For The Solar Collectors And Energy Storage. 2024.

9. Jopek H., Strek T. Optimization of the Effective Thermal Conductivity of a Composite / ed. Ahsan A. Rijeka: IntechOpen, 2011. P. Ch. 9.

10. Norouzi M., Amiri Delouei A., Seilsepour M. A general exact solution for heat conduction in multilayer spherical composite laminates // Compos. Struct. Elsevier Ltd, 2013. Vol. 106. P. 288–295.

11. Sihn S. et al. Enhancement of through-thickness thermal conductivity of sandwich construction using carbon foam // Compos. Sci. Technol. 2012. Vol. 72, № 7. P. 767–773.

12. Kang D.-Y., Jones C.W., Nair S. Modeling molecular transport in composite membranes with tubular fillers // J. Memb. Sci. 2011. Vol. 381, № 1. P. 50–63.

13. Wang H.M., Liu C.B. Analytical solution of two-dimensional transient heat conduction in fiber-reinforced cylindrical composites // Int. J. Therm. Sci. 2013. Vol. 69. P. 43–52.

14. Wei G. et al. Radiative heat transfer study on silica aerogel and its composite insulation materials // J. Non. Cryst. Solids. 2013. Vol. 362. P. 231–236.

15. Nield D.A., Bejan A. Convection in porous media. Springer, 2006. Vol. 3.

16. Yasuyuki T. et al. Three-dimensional natural convection in an inclined cylindrical annulus // Int. J. Heat Mass Transf. 1984. Vol. 27, № 5. P. 747–754.

17. Bu-Xuan W., Xing Z. Natural convection in liquid-saturated porous media between concentric inclined cylinders // Int. J. Heat Mass Transf. Elsevier, 1990. Vol. 33, № 5. P. 827–833.

18. Frederick R.L., Moraga S.G. Three-dimensional natural convection in finned cubical enclosures // Int. J. Heat Fluid Flow. 2007. Vol. 28, № 2.

19. Aziz K., Hellums J.D. Numerical solution of the three-dimensional equations of motion for laminar natural convection // Phys. Fluids. 1967. Vol. 10, № 2. P. 314–324.

20. Kayhani M.H., Norouzi M., Amiri Delouei A. A general analytical solution for heat conduction in cylindrical multilayer composite laminates // Int. J. Therm. Sci. 2012. Vol. 52. P. 73–82.